

Theory for all-optical responses in topological materials: the velocity gauge picture

Dasol Kim,^{1,2} Dongbin Shin,³ Alexandra S. Landsman,^{2,4} Dong Eon Kim,^{1,2,*} and Alexis Chacón^{1,2,†}

¹*Department of Physics and Center for Attosecond Science and Technology, POSTECH, 7 Pohang 37673, South Korea*

²*Max Planck POSTECH/KOREA Research Initiative, Pohang 37673, South Korea*

³*Max Planck Institute for the Structure and Dynamics of Matter and
Center for Free Electron Laser Science, 22761 Hamburg, Germany*

⁴*Department of Physics, Ohio State University, 191 West Woodruff Ave, Columbus, OH 43210, USA*

(Dated: May 27, 2021)

High Harmonic Generation (HHG), which has been widely used in atomic gas, has recently expanded to solids as a means to study highly nonlinear electronic response in condensed matter and produce coherent high frequency radiation with new properties. Most recently, attention has turned to Topological Materials (TMs) and the use of HHG to characterize topological bands and invariants. Theoretical interpretation of nonlinear electronic response in TMs, however, presents many challenges. In particular, the Bloch wavefunction phase of TMs has undefined points in the Brillouin Zone. This leads to singularities in calculating the inter-band and intra-band transition dipole matrix elements of Semiconductor Bloch Equations (SBEs). Here, we use the laser-electromagnetic velocity gauge $\mathbf{p} \cdot \mathbf{A}(t)$ to numerically integrate the SBEs and treat the singularity in the production of the electrical currents and HHG spectra. We use a prototype of Chern Insulators (CIs), the Haldane model, to demonstrate our approach. We find good qualitative agreement of the velocity gauge compared to the length gauge and the Time-Dependent Density Functional theory in the case of topologically trivial materials such as MoS₂. For velocity gauge and length gauge, our two-band Haldane model reproduces key HHG spectra features: (i) The selection rules for linear and circular light drivers, (ii) The linear cut-off law scaling and (iii) The anomalous circular dichroism. We conclude that the velocity-gauge approach captures experimental observations and provides theoretical tools to investigate topological materials.

I. INTRODUCTION

The measurement of the Quantum Spin Hall Effects (QSHEs) [1–5] in HgTe (2007) ushered a new era of condensed matter physics, paving the way for unexpected technological advances [3, 6, 7]. The HgTe material consists of quantum wells that exhibit transversal spin currents at the edge, but insulating features in the bulk under a static longitudinal voltage [6, 8] (see Fig. 1). These edge currents and insulating bulk suggest unique applications for TIs, including in metrology [9] and the control of quantum logic operations [10].

The quantum wells of HgTe, as well as other materials such as CdTe [2], have topological invariants belonging to the class \mathbb{Z}_2 of TIs. This is defined in terms of the wavefunction parities or Berry phase [2, 6]. This 2D TIs is a unique phase of matter in the sense that the edge (surface) current is protected by the *time-reversal symmetry* of the Hamiltonian and its *topological invariant* [11]. This symmetry protects against dissipation and provides robustness against perturbations of the topological materials [12].

Despite widespread interest in nonlinear interaction of topological materials with ultrafast laser pulses, there is little research on the topic due to the difficulties in theoretical modeling and interpretation of resulting higher harmonic emission. Addressing these challenges is instrumental to guiding future experimental observations

in TMs. In this paper, we expand the study of nonlinear optical emission to TMs by solving the SBEs in the laser-electromagnetic velocity gauge (VG) $\mathbf{p} \cdot \mathbf{A}(t)$ in the mid-infrared (MIR) laser regime. In particular, we introduce a new approach to address the integration of singularity in the SBEs for the highly non-linear optical response in the Topological Materials (TMs).

There is a wide variety of TMs depending on the *topological invariant* and the Hamiltonian symmetries of these materials. These classifications are organized in the periodic table of TMs (Insulators), shown in Ref. [6]. Depending on the dimensionality of the samples, symmetries, and topological invariant, this table shows TMs with charge currents, locked-spin up and down currents [13, 14], and Weyl fermions, among others. For instance, the QSHE leads to QSH insulators HgTe (2D TI) or Bi₂Se₃ (3D TI).

Haldane in 1988 introduced the first paradigmatic class of TMs that shows Quantum Anomalous Hall Effects (QAHEs) (see Appendix A). The Haldane model exhibits *quantized conductivities*, $\sigma_{xy} = \nu \frac{e^2}{h}$ at the edge, where e is the electron charge, h , the Plank constant and ν , the topological invariant (or the Chern Number). This invariant is a quantized integer number that characterizes topological CIs (see Fig. 1). The topological states have *singularities* in the BZ, which can lead to numerical problems (see Fig. 2 of Ref. [15]). Here, we treat these *singularities* by using the laser-electromagnetic velocity gauge (VG). As proof of concept, we use the Haldane model to test and validate this approach.

Figure 1(a) depicts the Quantum Hall Effect (QHE) without Landau levels [6, 12, 14]. This shows that ν is essential for topological materials. Moreover, this critical

* kimd@postech.ac.kr

† achacon@postech.ac.kr

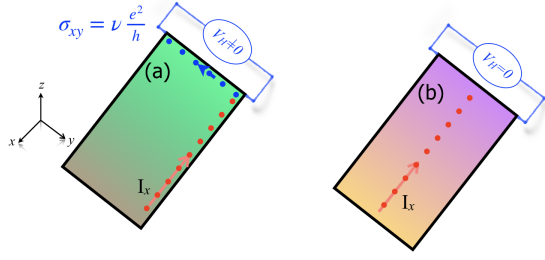


FIG. 1. Quantum Anomalous Hall Effect. Panel (a) depicts a cartoon of the longitudinal electrical currents I_x (red dots) and the *quantized transverse conductivity* $\sigma_{xy} = \nu \frac{e^2}{h}$ (Hall voltage $V_H \neq 0$ or charge current in blue dots) in an ideal Chern Insulator (CI) proposed by Haldane [14] (the Chern Number or topological invariant can be $\nu = \pm 1$), i.e. the Quantum Hall Effect without any applied external magnetic field. Panel (b), shows an example of traditional conductors which do not exhibit any quantized transverse Hall voltage ($V_H = 0$ or conductivity), $\nu = 0$.

aspect of TMs is contained in the undefined phase of the topological states. The singularity itself is independent of the wavefunction gauge, $|\tilde{u}_m^s\rangle = \exp(i\phi_m)|\tilde{u}_m^s\rangle$: the \mathbf{k} -position of the singular point can be manipulated via the gauge transformations, but no eliminated in TMs. The latter leads to an interconnection of the singularity in the wavefunction phase with ν [16]. Kohmoto showed that *without this singularity, no QHEs is observed* [16] and the material behaves as an ordinary semiconductor or conductor (see Fig. 1(b)). Unfortunately, this singularity of the wavefunction affects the calculation of the Chern number which is defined by [6, 12–14]:

$$\nu_m = \frac{1}{2\pi} \int_{\text{BZ}} d^2\mathbf{k} \cdot \mathbf{\Omega}_m(\mathbf{k}), \quad (1)$$

where $\mathbf{\Omega}_m(\mathbf{k}) = \langle \partial_{\mathbf{k}} u_{m,\mathbf{k}} | \times | \partial_{\mathbf{k}} u_{m,\mathbf{k}} \rangle = \nabla_{\mathbf{k}} \times \boldsymbol{\xi}_m(\mathbf{k})$ is the Berry curvature, the Berry connection, $\boldsymbol{\xi}_m(\mathbf{k}) = i \langle u_{m,\mathbf{k}} | \nabla_{\mathbf{k}} u_{m,\mathbf{k}} \rangle$ and the transition dipole matrix elements, $\mathbf{d}_{mn}(\mathbf{k}) = i \langle u_{m,\mathbf{k}} | \nabla_{\mathbf{k}} u_{n,\mathbf{k}} \rangle$. Hence, this singularity extremely complicates the calculations of the dipoles and Berry connections (see Ref. [15] and Fig. 2(a) in comparison to Fig. 2(b)).

On the other hand, the ultrafast non-linear optical spectroscopy and High Harmonic Generation (HHG) in topological materials are attracting the attention of ultrafast physics and condensed matter communities [17, 18]. This non-linear optical spectroscopy explores how *topological invariants* are encoded in the high harmonic spectrum, and is a complementary alternative to Angle-Resolved Photoelectron measurements [17, 19, 20]. However, the use of HHG to characterize TMs is very much in its infancy. A few recent studies of HHG in the paradigmatic Haldane model [17, 21, 22] have shown the complexity of computing the non-linear currents using the SBEs.

The evolutionary density matrix $\hat{\rho}(\mathbf{K}, t)$ or Semicon-

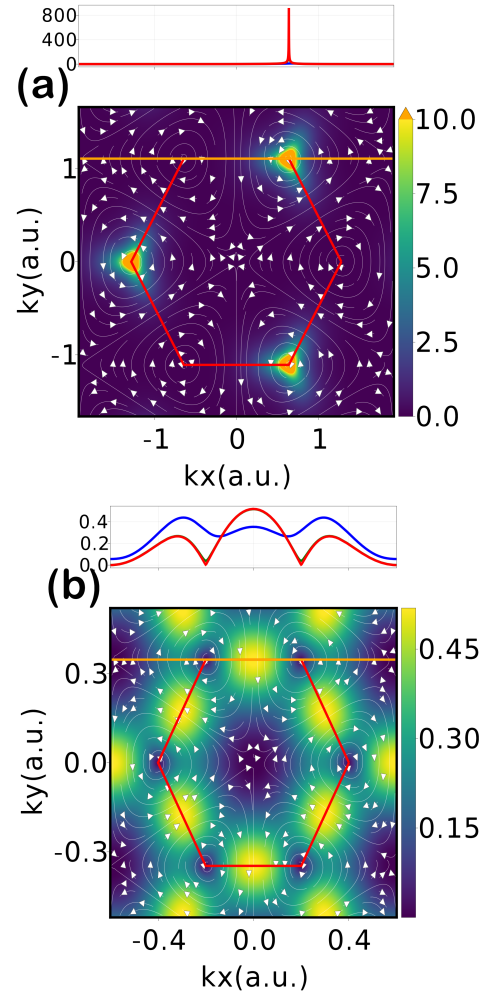


FIG. 2. Singularity in the Berry connection of topological material. (a) The absolute value of the Berry Connection for Chern insulators defined in the topological Haldane model and (b) same as in (a) but for a topologically trivial material, MoS₂. The vectorial field indicates how the Berry connection can accumulate a phase in the Haldane model. In other words, by the Stokes' Theorem, the topological Chern Number is $\nu_n = \frac{1}{2\pi} \oint_C \boldsymbol{\xi}_n(\mathbf{k}) \cdot d\mathbf{k}$, where C denotes a closed line-path integral. Upper panels show a 1D cross-section along the orange line for trivial and topological phase, i.e., the absolute value of Berry connection for small k_y -offsets, respectively.

ductor Bloch equations (SBEs) reads:

$$\begin{aligned} \frac{\partial}{\partial t} \hat{\rho}_{mn}(\mathbf{K}, t) = & -i \left[\varepsilon_{mn}(\mathbf{K} + \mathbf{A}(t)) - \frac{i}{T_2} \right] \hat{\rho}_{mn}(\mathbf{K}, t) \\ & - i \mathbf{E}(t) \cdot [\mathbf{D}(\mathbf{K} + \mathbf{A}(t)), \hat{\rho}(\mathbf{K}, t)]_{mn}. \quad (2) \end{aligned}$$

The above equation contains the singular term of the topological wavefunction: the Berry connection and the dipole matrix element which are encoded in $\mathbf{D}_{mn}(\mathbf{k})$ [15] (see below for mathematical definition). This $\mathbf{D}_{mn}(\mathbf{k})$ contains both the inter-band dipole matrix element $\mathbf{d}_{mn}(\mathbf{k})$ for $m \neq n$, and the intra-band Berry connection $\boldsymbol{\xi}_m(\mathbf{k})$ for $m = n$. Here $\mathbf{A}(t) = -\partial_t \mathbf{E}(t)$ is the vector potential of the electric field $\mathbf{E}(t)$, and the energy difference

between the m^{th} and n^{th} bands, $\varepsilon_{mn}(\mathbf{k}) = \varepsilon_m(\mathbf{k}) - \varepsilon_n(\mathbf{k})$. We use the so called moving BZ frame [23], $\mathbf{k} = \mathbf{K} + \mathbf{A}(t)$, and the phenomenological dephasing time T_2 . The singularities in $\mathbf{D}_{mn}(\mathbf{k})$ in Eq. (2) induces numerical errors in the calculation of high-order harmonics from TMs, more noticeable in strong field regimes. These lead to *wrong plateau* and *cut-off structures* of the HHG spectra (see Ref. [15]), if the singular integral in Eq. (2) is not handled properly.

To address this problem, we previously developed (a) the variable ‘‘matter-gauge wavefunctions’’ method, which considers the pseudo-spin gauge Hamiltonian and the periodicity of the Haldane model in the BZ [15]. This method showed an excellent resolution of the harmonic orders (HOs) and cut-off of the HHG spectra. Additionally, theoretical efforts by Silva et al. [24] handled this singularity by using (b) the time-evolution of $\hat{\rho}(\mathbf{k}, t)$ in the Maximally Localized Wannier basis (MLWB).

Each method, either (a) or (b) has its advantages and disadvantages. For instance, in Ref. [15], method (a) only works in the case of Tight Binding Approximations (TBAs). In Ref. [24], method (b) has the disadvantage in the evaluation of the dephasing time at each time-step t . The evaluation of T_2 makes its numerical implementation tedious for straightforward technical development compared to the VG. The MLWB method requires evaluations of T_2 in the Hamiltonian-gauge instead of its original Hamiltonian-Wannier-gauge representation (increasing the number of computational operations). Note, we have verified that both methods (a) and (b) reach the same results in the Hamiltonian Bloch basis.

Theoretical study on the laser-electromagnetic gauge symmetry in trivial materials can be found in Ref. [25]. This prominent study found gauge invariance of the non-linear optical responses only under a specific number of bands. The truncation of the SBEs solution as a function of number of bands breaks the gauge-symmetry [25] in the calculation of the charge currents (see Appendix B).

We introduce the laser-electromagnetic velocity gauge to compute the SBEs and the electrical currents in trivial materials and TMs. Furthermore, we compare the HHG spectra produced by the proposed VG with the length gauge (LG). The rest of the paper is organized as follows: In Section (II), we describe the electrical current and derive the SBEs in the laser-electromagnetic length gauge and velocity gauge. In section (III), we use the VG to calculate high harmonic emission from trivial material such as a monolayer of MoS₂. To confirm the validity of our approach, we compare these results with the LG and the Time-Dependent Density Functional Theory (TDDFT) for MoS₂. We then extend the application of the proposed VG theoretical framework to topological Chern Insulators (CIs) for both linearly and circularly polarized MIR or THz light sources. Our approach is further validated by computing the cut-off law [26] of the HHG spectra and the Circular Dichroism in topological materials. We also compare these outcomes with the length gauge results. In Section (IV), we discuss the advantages and disadvantages of LG and VG pictures in

computing the HHG spectra and conclude that VG is a suitable and straight-forward method to calculate the HHG spectra from topological materials.

II. THEORETICAL FRAMEWORK

In the dipolar approximation, the velocity gauge, and length gauge are theoretically used to describe the non-linear optical responses [27–29] from solids subjected to ultrashort lasers. The total Hamiltonian of the laser-lattice system is $\hat{H}(t) = \hat{H}_0 + \hat{V}_{\text{int}}(t)$, the interaction term $\hat{V}_{\text{int}}(t)$ in the VG or LG theoretical framework reads:

$$\hat{V}_{\text{int}}^{(\text{VG})} = \hat{\mathbf{p}} \cdot \mathbf{A}(t) + \mathbf{A}^2(t)/2, \text{ and} \quad (3)$$

$$\hat{V}_{\text{int}}^{(\text{LG})} = \hat{\mathbf{x}} \cdot \mathbf{E}(t). \quad (4)$$

Although these laser-electromagnetic gauges should provide the same results for a physical observable, for instance, the HHG spectra, previous studies have found that, unfortunately, it is not the case in several systems [29–31]. This breaking of the gauge-symmetry occurs when an approximation is carried out to solve the Time-Dependent Schrödinger Equation (TDSE). Note, however, that the full numerical integration of the TDSE for the HHG spectra under the LG and VG is covariant [32, 33]. This supports the observation that any approximation of the TDSE can break the laser-electromagnetic gauge-symmetry. For instance, in the Strong Field Approximation (SFA) applied to a gas, this laser-electromagnetic gauge-symmetry is broken [34]; producing different HHG spectra, particularly for the emitted intensity yield [30, 31]. Nevertheless, the main qualitative features of the high harmonics are reproduced by the LG and VG in the SFA formalism. In the case of TMs, we expect a similar trend.

In the length gauge, the numerical integration of the SBEs is an extremely problematic task: the \mathbf{k} -space position operator depends on the crystalline momentum derivatives $i\partial_{\mathbf{k}}$ in the BZ (see Eq. (10)). Numerically, this finite \mathbf{k}_j -neighbor will couple non-define SBEs, including the electronic density and electron coherence of the $\hat{\rho}(\mathbf{k}, t)$ operator, near the singular point of the Berry connection and dipoles. This problem has been found not only in topological materials but also in trivial Ref. [35].

On the contrary, the velocity gauge offers a way to avoid the singularity issue by the de-coupling of the neighboring \mathbf{k}_j . Hence, notwithstanding some disadvantages of the VG, related to the Bloch acceleration theorems [27–29] and crystal kinetic momenta, it offers an attractive alternative to the typically used length gauge. We therefore propose the velocity gauge as an alternative to the LG to study the non-linear optical responses from topological materials.

A. Velocity gauge picture

Commonly, in a periodic crystalline structure subjected to an external laser-field, the charge current is calculated by integrating the \mathbf{k} -elementary-microscopic currents in the BZ:

$$\mathbf{J}(t) = \int_{\text{BZ}} \frac{d^3k}{(2\pi)^3} \mathbf{j}(\mathbf{k}, t). \quad (5)$$

Here we define the elementary-microscopic current $\mathbf{j}(\mathbf{k}, t)$ as

$$\begin{aligned} \mathbf{j}(\mathbf{k}, t) &= -\text{Tr}(\hat{\rho}\hat{\mathbf{v}}) \\ &= \text{Tr}(\hat{\rho}(\mathbf{k}, t)\hat{\mathbf{p}}) - N_{\text{VB}}\mathbf{A}(t) \\ &= -\sum_{m,n} \rho_{mn}(\mathbf{k}, t)\mathbf{P}_{nm}(\mathbf{k}) - N_{\text{VB}}\mathbf{A}(t). \end{aligned} \quad (6)$$

This corresponds to the expectation value of the *velocity operator* $\hat{\mathbf{v}} = -i[\hat{H}(t), \hat{\mathbf{x}}]$. The current $\mathbf{j}(\mathbf{k}, t)$ is defined in terms of the density matrix $\hat{\rho} = \hat{\rho}(\mathbf{k}, t)$, the momentum matrix element \mathbf{P} , and the number of valence band N_{VB} [28, 29, 35].

The time-propagation of the density matrix $\hat{\rho}(\mathbf{k}, t)$ is given by Liouville-von Neumann equation,

$$i\frac{\partial\hat{\rho}(\mathbf{k}, t)}{\partial t} = [\hat{H}(t), \hat{\rho}(\mathbf{k}, t)], \quad (7)$$

where $\hat{\rho}$ will be evaluated in the VG via $\hat{H}(t)$.

1. Hamiltonian representation in the VG

Usually, the Hamiltonian representation is defined by the Bloch states for the laser-free Hamiltonian, \hat{H}_0 . In the VG, the Hamiltonian describing the laser-periodic crystalline interaction reads:

$$\hat{H}(t) = \hat{H}_0 + \hat{\mathbf{p}} \cdot \mathbf{A}(t). \quad (8)$$

We neglect the term proportional to $A^2(t)$ of the interacting $\hat{V}_{\text{int}}^{(\text{VG})}(\mathbf{k}, t)$ of Eq. (3) (for details, see Ref. [28]). Thus, the time-momentum evolution of the density matrix elements in the VG reads,

$$\begin{aligned} \dot{\rho}_{mn}(\mathbf{k}, t) &= -i\left[\varepsilon_{mn}(\mathbf{k}) - i\frac{1}{T_2}\right]\rho_{mn}(\mathbf{k}, t) \\ &-i\mathbf{A}(t) \cdot \sum_l [\mathbf{P}_{ml}(\mathbf{k})\rho_{ln}(\mathbf{k}, t) - \mathbf{P}_{ln}(\mathbf{k})\rho_{ml}(\mathbf{k}, t)]. \end{aligned} \quad (9)$$

Here $\varepsilon_{mn}(\mathbf{k})$ is the energy difference between the band m and n , with the phenomenological dephasing time given by T_2 .

The advantage of the VG is that every \mathbf{k} -crystal momentum channel is de-coupled [28, 29]. Hence one can choose a discretized \mathbf{k} -grid that avoids the singularity. Additionally, we can quickly parallelize the implementation of the code for Eq. (9). For instance, we use Message Passing Interface (MPI) in C++ and numerically solve Eq. (9) using Runge-Kutta 5th order method.

B. Length gauge pictures

The evolution of the electronic density operator $\hat{\rho}(\mathbf{k}, t)$ in length gauge and the ‘‘Hamiltonian matter-gauge’’ can be acquired in a similar procedure as described in Refs. [15, 28, 29]. From Liouville-von Neumann equation given by Eq. (7), considering the interacting potential of Eq. (4) and the position operator in the Bloch basis $\hat{\mathbf{x}}$ [36]:

$$\hat{\mathbf{x}}_{mn} = (-i\nabla_{\mathbf{k}} + \boldsymbol{\xi}_m)\delta_{mn} + \mathbf{d}_{mn}, \quad (10)$$

$\hat{\rho}(\mathbf{k}, t)$ can be expressed as Eq. (2). This representation is sensitive to the singularity of the topological states in TMs, as already discussed above. The position operator indeed contains intra-band momentum terms, which are defined in $\nabla_{\mathbf{k}}$. In a finite and a discretized \mathbf{k} -space grid, this means that the $\hat{\rho}(\mathbf{k}, t)$ depends on its \mathbf{k} -space ‘‘numerical neighbour cell’’ and the electric field strength. This is problematic in LG and in its Hamiltonian representation. Even in the case that one can express the time-evolution of $\hat{\rho}(\mathbf{K}, t)$ in terms of the moving frame $\mathbf{k} = \mathbf{K} + \mathbf{A}(t)$ [15, 23, 37], the vector potential $\mathbf{A}(t)$ will force the $\hat{\rho}(\mathbf{K}, t)$ to travel throughout the singularity described in Fig. 2(a) for TMs.

1. Wannier representation for the LG

The numerical solution to Eq. (2) requires continuous quantities such as transition dipole matrix elements and Berry connections. Unfortunately, this is not possible for topological materials [15, 16]. The Wannier representation [38] promises to address this problem. From the application of Eq. (7), considering TBA as a basis and Eq. (2), the density equation of motion in the Wannier basis yields [38]:

$$\begin{aligned} i\frac{\partial}{\partial t}\hat{\rho}^{(\text{W})}(\mathbf{K}, t) &= [\hat{H}_0^{(\text{W})}(\mathbf{K} + \mathbf{A}(t)), \hat{\rho}^{(\text{W})}(\mathbf{K}, t)] \\ &+ \mathbf{E}(t) \cdot [\mathbf{D}^{(\text{W})}(\mathbf{K} + \mathbf{A}(t)), \hat{\rho}^{(\text{W})}(\mathbf{K}, t)]. \end{aligned} \quad (11)$$

Here, $\hat{H}_0^{(\text{W})}(\mathbf{k})$ is expressed in the TBA Hamiltonian. $\mathbf{D}^{(\text{W})}(\mathbf{k})$ and $\hat{\rho}^{(\text{W})}(\mathbf{k}, t)$ are dipole matrix and density matrix in Wannier basis. $\mathbf{D}^{(\text{W})}(\mathbf{k})$ is calculated by

$$\mathbf{D}_{nm}^{(\text{W})}(\mathbf{R}) = \sum_{\mathbf{R}'} e^{i\mathbf{k}\cdot\mathbf{R}'} \langle \mathbf{0}n | \hat{\mathbf{r}} | \mathbf{R}m \rangle. \quad (12)$$

This exhibits continuous dipoles even in case of topological materials. Furthermore, if we assume that $\mathbf{D}^{(\text{W})}(\mathbf{k})$ is diagonal, for instance:

$$\langle \mathbf{0}n | \hat{\mathbf{r}} | \mathbf{R}m \rangle = \delta_{\mathbf{0}\mathbf{R}}\delta_{nm}\boldsymbol{\Delta}_n, \quad (13)$$

one can treat $\mathbf{D}^{(\text{W})}(\mathbf{k})$ as a \mathbf{k} -independent term [39]. Here $\boldsymbol{\Delta}_n = \langle \mathbf{0}n | \hat{\mathbf{r}} | \mathbf{0}n \rangle$ is the center of n^{th} Wannier function or can be understood as a position of the corresponding atomic orbital.

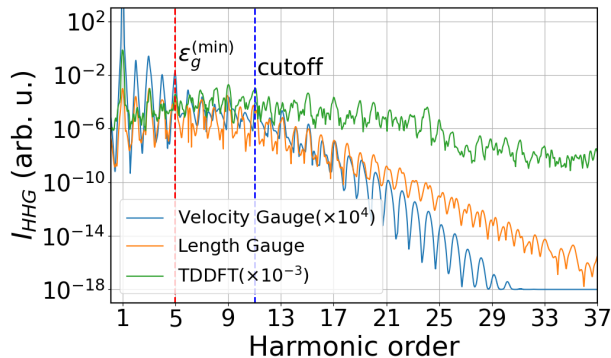


FIG. 3. Calculated HHG spectra from MoS₂ by the SBEs in the length gauge (orange line), velocity gauge (blue line) and TDDFT (green line). Our laser parameters are $\hbar\omega_0 = 0.3626$ eV, peak electric field $E_0 = 0.01265$ a.u. and time pulse duration at Full-Width at Half Maximum (FWHM) of 14 opt. cycles under a gaussian envelope, with dephasing time $T_2 = 2.7$ fs. To mimic the band structure of MoS₂, we used $M_0 = 0.9$ eV = 0.0331 a.u., $t_1 = 0.4$ eV = 0.0147 a.u., $t_2 = 0.667$ eV = 0.0245 a.u., and $\phi_0 = 0$ rad for Haldane model parameters. Red dotted line indicates band gap of the MoS₂ which is 1.8 eV.

III. NUMERICAL RESULTS AND VALIDATIONS

Our velocity gauge approach is first validated in a topologically trivial material. Subsequently, we extend the VG approach to the paradigmatic Haldane model. In the case of trivial materials, we also calculate the HHG spectra in the length gauge and the TDDFT [40], and then compare it to the VG results. For the trivial material, we use a simplified two-bands TBA of monolayer MoS₂. In other words, we adjust the TBA parameters to reproduce the minimum energy gap and maximum energy gap of MoS₂ (for details, see Appendix A). We simulate the HHG spectrum using VG and LG via Eqs. (9) and (11), respectively.

Figure 3 shows HHG signals for both gauges in the trivial phase of MoS₂. The spectrum produced by the VG is qualitatively similar in essential features to the LG and the TDDFT calculations. For example, the VG plateau with even and odd HO structures and cut-off have a good qualitative agreement with the other two methods. For better visualization, all three calculations are normalized to have similar low-order harmonics yields.

The LG and VG will yield identical results [41], if and only if the full eigenstates and eigen energies of the Hamiltonian $H_0^{(w)}$ are considered in the simulation and the sum rule in Appendix B is satisfied. Moreover, since we use TBA up to two states and the second nearest neighbor hopping for the Hamiltonian $H_0^{(w)}$, the HHG calculations can break the laser-electromagnetic gauge-symmetry. This effect is similar to the HHG in gases.

The difference between both gauges in comparison to the TDDFT can be explained by several factors, such as

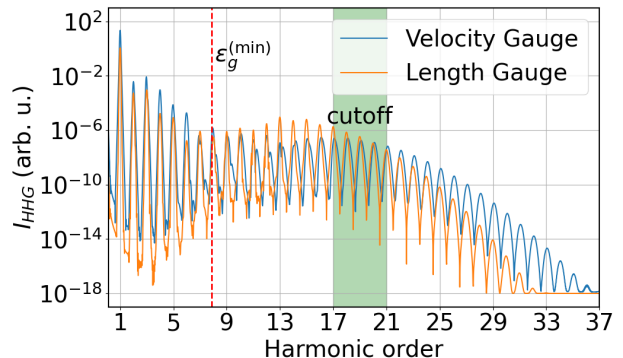


FIG. 4. Calculated HHG spectra from Chern insulator in the length and velocity gauges. Laser central frequency $\omega_0 = 0.38$ eV, peak electric field $E_0 = 0.0045$ a.u. and FWHM duration of 14 cycles under a gaussian envelope are used. For dephasing time $T_2 = 5.3$ fs is used. The Chern insulator has $M_0 = 0.0635$ a.u., $t_1 = 0.075$ a.u., $t_2 = 0.025$ a.u., and $\phi_0 = 1.16$ rad for Haldane model parameters. Red dotted line indicates band gap of material which is 3.0 eV.

the incomplete sum rule between position and momentum operator in Eq. (B1) of Appendix (B). The incomplete basis set of TBA breaks this commutation relation, and of course the gauge-symmetry too. For solids described in the plane-wave basis, it has been proven that the VG requires up to the 30th band to obtain convergence [42], compared to two-bands in LG. Another origin of the difference between the VG and the LG is the action of the dephasing time T_2 in $\hat{\rho}(\mathbf{k}, t)$. This phenomenological variable plays a different role in the two gauges (for details, see Appendix C). Note, however, that our HHG spectra show a similar tendency in both gauges; for example, the plateau structure and cut-off are similar in the VG and LG (See Fig. 3).

A. Topological nonlinear optical response: the velocity gauge

We now extend the VG model to topological materials. The Haldane model (HM) belongs to the first class of topological Chern Insulators (CIs). We use the topological HM to study non-linear optical emissions and charge currents induced by the laser-CI interactions. This prototype of CI will test our velocity gauge approximation in TMs by comparing our HHG simulations in the VG to the LG.

The total HHG spectra produced by linearly-polarized MIR laser for the LG and VG are in Fig. 4. We can qualitatively find good agreement between the HHG spectrum produced by the VG and LG. Surprisingly, even in this two-band toy model, our VG approach can reproduce the key features of HHG in TMs. In particular, the selection rules produced by the VG for the HOs in (i) the perturbative region (low HOs of the HHG-spectra), (ii) the plateau (middle part of the HHG spectra), and (iii)

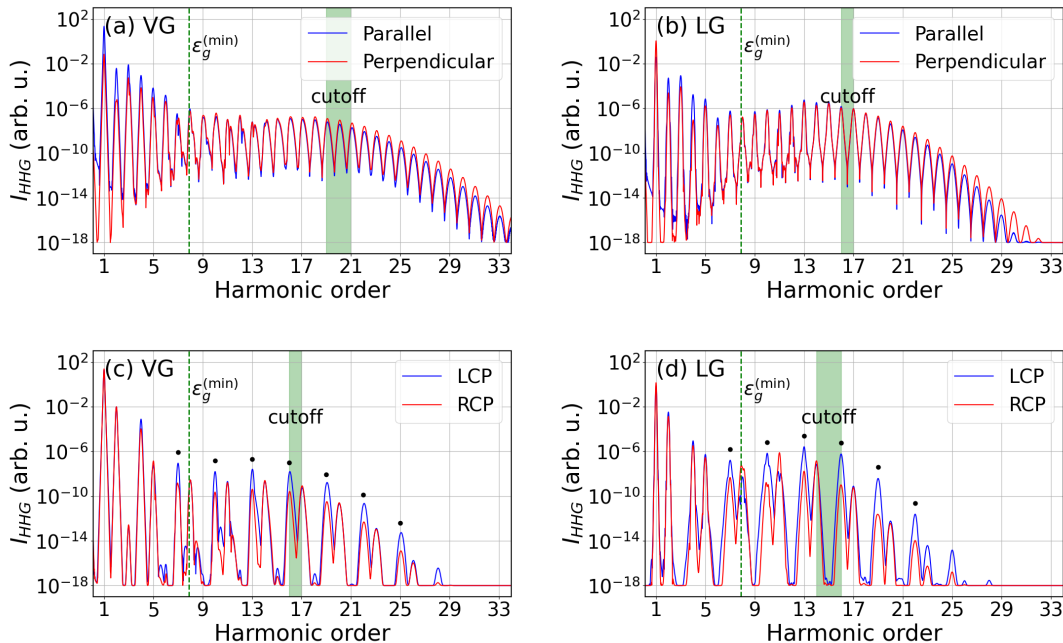


FIG. 5. Selection rules of the HHG spectra for the VG and LG in Chern insulators. (a-b) Shows calculated HHG spectrum using linearly-polarized laser along Γ -K direction. Harmonic spectra along parallel or perpendicular direction relative to laser polarization are illustrated. (c-d) shows total harmonic spectra, $I_{\text{HHG}}(\omega) = \omega (|J_x(\omega)|^2 + |J_y(\omega)|^2)$, produced by circularly-polarized lasers. Results from the right-hand/left-hand circularly-polarized laser (RCP/LCP) are shown. Laser parameters given by: central frequency $\hbar\omega_0 = 0.38$ eV, peak electric field $E_0 = 0.0045$ a.u. and FWHM duration of 14 opt. cycles under a gaussian envelope. For dephasing time $T_2 = 5.3$ fs is used. The cut-offs of the HHG spectra are on green shadows. The black dots indicate co-rotating harmonics for the calculation of CD. The vertical dashed lines show the bandgap of the topological material.

the cut-off (HO to which the subsequent photon-energies drastically decrease its intensity yield) show good agreement with results from the LG (see Fig. 5(a) and (b)).

In Fig. 5, a detailed comparison between the HHG spectra in the VG and the LG is performed. Since time-reversal symmetry and inversion symmetry are broken in the HM, even harmonics and odd harmonics can be seen in the HHG spectrum [19] along directions both perpendicular and parallel to laser polarization. This result is gauge-symmetric, appearing both in the LG and the VG, as can be seen in Figs. 5(a) and 5(b).

Another interesting test for the VG approach is the calculation of the Circular Dichroism (CD) produced from the HHG signal of the CIs (for details, see Ref. [15]). The HHG spectra are produced by left-hand and right-hand circularly polarized lasers. We define the Circular Dichroism (CD) as the normalized difference between HOs from the left circularly-polarized laser (LCP) and right circularly-polarized laser (RCP),

$$\text{CD}_k = \frac{I_{\text{RCP}}^k - I_{\text{LCP}}^k}{I_{\text{RCP}}^k + I_{\text{LCP}}^k}. \quad (14)$$

Note that for materials that preserves the time-reversal symmetry, such as MoS_2 , CD_k is zero.

Figures 5(c) and 5(d) show HHG spectra produced by the VG and LG formalisms. The co-rotating HOs, $k = 3n + 1$, produced by LCP are much larger than the

co-rotating HOs produced by the RCP driver. We observe that for all co-rotating HOs, the $\text{CD} = -1$, for HM parameters with $\nu = -1$. This is observed for both the VG and LG pictures, and is consistent with the previously reported physics of TMs Ref. [15].

We now check whether the cut-off linear scaling law of the HHG spectrum can be verified within the VG approach [26]. The Harmonic spectra as a function of electric field peak strength are shown in Fig. 6. Both the VG and LG show a similar linear cut-off law: the cut-off of HHG spectra as a function of the electric field strength E_0 is a straight line. Finally, we show the occupation of the conduction band as a function of time in Fig. 7 around $k_y = 0$ (see Fig. 9 for a plot in k -space).

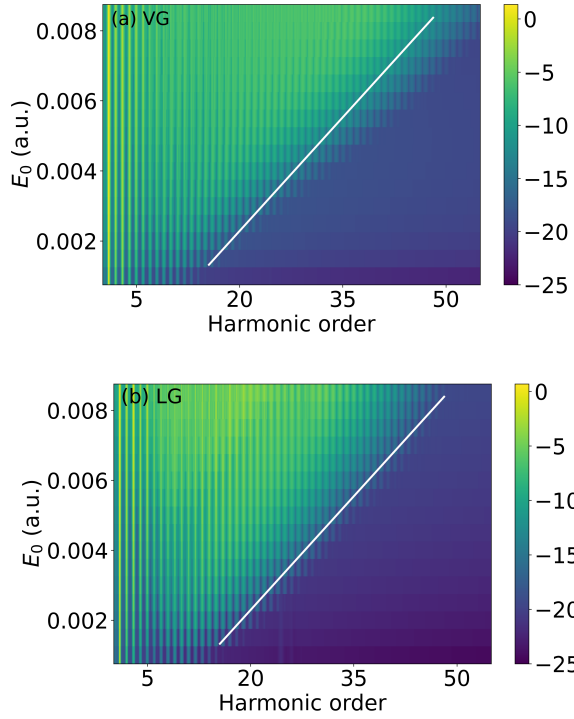


FIG. 6. Cutoff law for Chern insulators in both velocity and length gauges. Total HHG emissions, $I_{\text{HHG}}(\omega) = \omega (|J_x(\omega)|^2 + |J_y(\omega)|^2)$ as a function of electric field peak strength E_0 for (a) VG and (b) LG for linearly polarized light. Other laser parameters are the same as in Fig. 5. Both velocity and length gauges show linear scaling of the high harmonic cutoff with peak electric field.

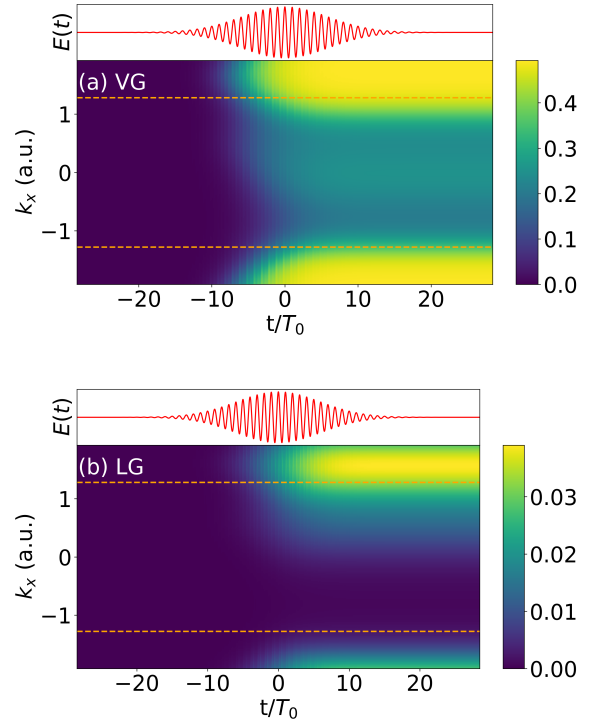


FIG. 7. Time-evolution of the "cross-section" in the conduction band occupation. Occupation integrated along k_y is shown as a function of time. k_x axis is along $K' - \Gamma - K$ direction (see Fig. 9), and orange dotted line indicates the K and K' point in Brillouin zone.

IV. CONCLUSIONS

We conclude that the laser-electromagnetic velocity gauge approach can successfully *integrate the numerical singularity in the Berry connection of topological materials* and reproduce key features of the high harmonic spectrum. Using a toy two-band model, we show that the velocity gauge can qualitatively capture the charge current and the HHG spectra without any artificial noise introduced by the singularity of the transition matrix elements, either dipole, Berry connection, or momentum.

Additionally, we compare our results: (1) HHG spectra produced from linearly and circularly polarized lasers, (2) the Circular dichroism, (3) the linear cut-off law; to those produced by the length gauge (LG) in the maxima localized Wannier basis. We find good qualitative agreement in the high harmonics spectrum between the VG and the LG, both in trivial and topological materials. The lack of quantitative agreement between the two approaches is partly due to the limited number of bands and the tight-binding approach, which we used as a proof of concept.

We expect the VG approach to be more rigorous for TMs, since it treats the numerical singularity present within the LG approach. Hence the velocity gauge approach presented here introduces new theoretical tools in investigating the highly nonlinear optical emission from topological materials.

ACKNOWLEDGMENTS

We thank professor Angel Rubio's group for calculating the TDDFT result for MoS₂. D.K., D.E.K and A.C. acknowledge support by Max Planck POSTECH/KOREA Research Initiative Program [Grant No 2016K1A4A4A01922028] through the National Research Foundation of Korea (NRF) funded by the Ministry of Science, ICT & Future Planning, partly by the Korea Institute for Advancement of Technology (KIAT) grant funded by the Korea Government (MOTIE) (P0008763, The Competency Development Program for Industry Specialist). D.S. is supported by Alexander von Humboldt Foundation. A.S.L acknowledges support by the Institute for Materials Research (IMR) at Ohio State University and Center of Emergent Materials (CEM) supported by NSF, grant No. DMR-2011876.

APPENDIX

Appendix A: The Haldane model

The Haldane model (HM) [14] is the first model representing the quantum anomalous Hall effect (QAHE) introducing local magnetic flux. This model is a minimum of a two-band toy model but captures the most relevant physics of the Chern insulator. The HM considers a TBA

Hamiltonian in a hexagonal lattice and hopping parameters up to the next-nearest neighborhood (NNN).

This model can be a Chern insulator or a trivial insulator, depending on its parameter.

1. Haldane's Hamiltonian

The Haldane model is a two-band approximation obtained from a hexagonal lattice of two sub-lattices with atoms A and B. Thus, after applying the TBA for on-site potentials, the nearest-neighbor (NN) and the next-to-nearest-neighbor (NNN), and changing the Hamiltonian elements from Wannier function to Bloch basis, we find,

$$H_0(\mathbf{k}) = B_0(\mathbf{k})I + \mathbf{B}(\mathbf{k}) \cdot \boldsymbol{\sigma}, \quad (\text{A1})$$

here, I is the identity matrix and $\boldsymbol{\sigma} = \{\sigma_x, \sigma_y, \sigma_z\}$ Pauli's matrices. Additionally, the $\mathbf{B}(\mathbf{k}) = \{B_1(\mathbf{k}), B_2(\mathbf{k}), B_3(\mathbf{k})\}$ is known as pseudomagnetic field. Each vector is

$$B_0(\mathbf{k}) = 2t_2 \cos \phi_0 \sum_{i=1}^3 \cos(\mathbf{k} \cdot \mathbf{b}_i), \quad (\text{A2})$$

$$B_1(\mathbf{k}) = t_1 \sum_{i=1}^3 \cos(\mathbf{k} \cdot \mathbf{a}_i), \quad (\text{A3})$$

$$B_2(\mathbf{k}) = t_1 \sum_{i=1}^3 \sin(\mathbf{k} \cdot \mathbf{a}_i), \quad (\text{A4})$$

$$B_3(\mathbf{k}) = M_0 - 2t_2 \sin \phi_0 \sum_{i=1}^3 \sin(\mathbf{k} \cdot \mathbf{b}_i), \quad (\text{A5})$$

where \mathbf{a}_i are the NN vectors, and \mathbf{b}_i the NNN vectors.

The displacement vectors are given by $\mathbf{a}_1 = (0, a_0)$, $\mathbf{a}_2 = \frac{1}{2}(-\sqrt{3}, -1)a_0$, $\mathbf{a}_3 = \frac{1}{2}(\sqrt{3}, -1)a_0$, $\mathbf{b}_1 = (\sqrt{3}, 0)a_0$, $\mathbf{b}_2 = \frac{1}{2}(-\sqrt{3}, +3)a_0$ and $\mathbf{b}_3 = \frac{1}{2}(-\sqrt{3}, -3)a_0$.

where t_1 is the NN hopping parameter and t_2 , the NNN hopping parameter. M_0 is on-site potential that breaks the inversion symmetry, and ϕ_0 the local magnetic flux, which breaks the time-reversal symmetry.

Figure 8 shows the topological phase diagram of HM. The Haldane model yields a gapless band structure, where the topological phase transition occurs, with the condition $M_0/t_2 = \pm 3\sqrt{3} \sin \phi_0$.

HM can have three topological invariants or Chern numbers or topological phases $\nu = \{-1, 0, +1\}$, where $\nu = 0$ is trivial insulator (or "Dirac Semimetal") and $\nu = \pm 1$ is topological non-trivial phase.

As shown in Fig. 8, the topological phase is determined by ϕ_0 and M_0/t_2 . t_1 . These parameters affect band structure but do not affect the topological phase. By controlling those parameters, we can adjust the bandgap and topological phase to mimic a topological CI.

2. Dipoles, Berry connection, Berry Curvature and Chern number

Fortunately, we can solve 2x2 Hamiltonian analytically. The energy dispersion of the Haldane model reads,

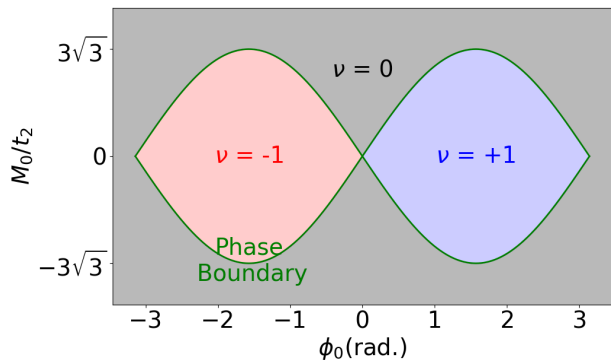


FIG. 8. Topological phase diagram for the Haldane model. The diagram shows three different topological phases $\nu = \{0, \pm 1\}$, where $\nu = 0$ indicates topologically trivial state and $\nu = \pm 1$ represents Chern insulator.

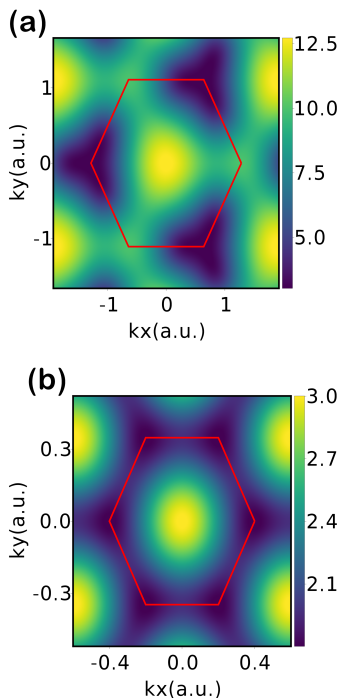


FIG. 9. Energy dispersion for the Haldane model. Band gap (eV) for (a) Chern insulator used in the calculation and (b) trivial material, MoS₂. As time-reversal symmetry is broken, (a) shows different bandgap in K' and K point while (b) has the same bandgap.

$$\varepsilon_{c/v}(\mathbf{k}) = B_0(\mathbf{k}) \pm |\mathbf{B}(\mathbf{k})|. \quad (\text{A6})$$

The band-gap for HM is shown in Fig. 9. Here we use parameters $M_0 = 0.0635$ a.u., $t_1 = 0.075$ a.u., $t_2 = 0.025$ a.u., and $\phi_0 = 1.16$ rad for topological material. For trivial material, MoS₂, $M_0 = 0.9$ eV = 0.0331 a.u., $t_1 = 0.4$ eV = 0.0147 a.u., $t_2 = 0.667$ eV = 0.0245 a.u., and $\phi_0 = 0$ are used.

To investigate topological aspects of materials, it is required to calculate the dipole matrix elements,

$$\mathbf{d}_{m'm}(\mathbf{k}) = i\langle u_{m',\mathbf{k}} | \nabla_{\mathbf{k}} | u_{m,\mathbf{k}} \rangle, \quad (\text{A7})$$

where $|u_{m,\mathbf{k}}\rangle$ is the periodic part of Bloch state. Usually, people distinguish diagonal and off-diagonal components in Eq. (A7) and call diagonal components as Berry connection,

$$\begin{aligned} \xi_m(\mathbf{k}) &= \mathbf{d}_{mm}(\mathbf{k}) \\ &= i\langle u_{m,\mathbf{k}} | \nabla_{\mathbf{k}} | u_{m,\mathbf{k}} \rangle. \end{aligned} \quad (\text{A8})$$

Berry connection and off-diagonal dipole are plotted in Figs. 2 and 10. The dipole matrix element shows an interesting vortex structure in topological and trivial phases, which might lead to totally different coupling with the linearly and elliptically polarized lasers (see K' points in Fig. 10(a) vs. Fig. 10(b)).

The Berry connection has singularity while the off-diagonal dipole “only has discontinuity” (see Fig. 2(a)). Moreover, the dipole absolute value is gauge-invariant and has no discontinuity (see Figs. 10(a)). Although, the Berry connection is gauge dependent the curl of the Berry connection (called as the Berry curvature):

$$\Omega_m(\mathbf{k}) = \nabla_{\mathbf{k}} \times \xi_m(\mathbf{k}) \quad (\text{A9})$$

is gauge invariant. The integration of the Berry curvature over Brillouin zone,

$$\nu_m := \frac{1}{2\pi} \int_{\text{BZ}} \Omega_m(\mathbf{k}) \cdot d^2\mathbf{k}, \quad (\text{A10})$$

is a *topological invariant* of the system, called Chern number, which is shown in Fig. 8.

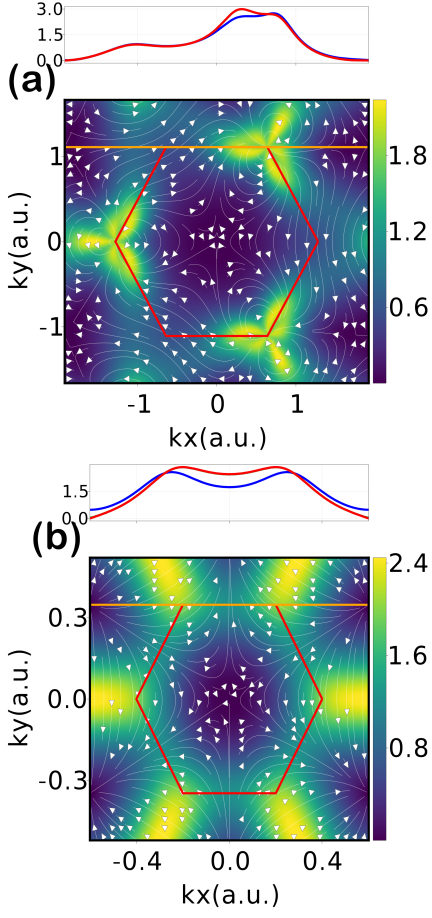


FIG. 10. Dipole matrix element for topological materials. (a) Real value of the dipole matrix element for Chern Insulators defined in the topological Haldane model and (b) same as in (a) but for a topologically trivial material, i.e., MoS₂. The vectorial field indicates real components of the dipole matrix element. Upper panels show it cut along the orange line, i.e., the real value of dipole is plotted along the orange line with small k_y offsets. Euclidean norm of dipole's real value is smooth for both cases, but the non-trivial topological case (a) has vortex while (b) has no discontinuity.

Appendix B: Gauge covariance

1. Sum rule for gauge covariance

It is well-known that VG needs more bands to get convergence with LG. The main problem is that canonical commutation relation

$$[\hat{x}^\alpha, \hat{p}^\beta] = i\delta_{\alpha\beta}, \quad (\text{B1})$$

where $\{\alpha, \beta\} = \{x, y, z\}$, is generally not valid when we have finite bands [27–29, 43].

In the plane wave basis, we can numerically satisfy this relation by increasing the number of bands up to the convergence. In TBA, however, we can not state that more bands always give better results given the constrain of Eq. (B1).

Furthermore, from the definition of $\hat{\mathbf{x}}$, and the Heisenberg relationship with the evolution of given operator, the momentum matrix reads,

$$\hat{\mathbf{P}} = \frac{\partial \hat{H}_0}{\partial \mathbf{k}} - i[\hat{\mathbf{D}}, \hat{H}_0]. \quad (\text{B2})$$

If we use the Hamiltonian gauge, H_0 becomes a diagonal matrix of energy dispersion [39, 44]. Then, Eq. (B4) becomes the well-known formula [25, 39],

$$\mathbf{P}_{mn} = \begin{cases} \frac{\partial}{\partial \mathbf{k}} \varepsilon_m & \text{if } m = n, \\ i(\varepsilon_m - \varepsilon_n) \mathbf{d}_{mn} & \text{if } m \neq n \end{cases}, \quad (\text{B3})$$

in which the first term is the intra-band component, and other terms define the inter-band currents.

In Wannier representation, H_0 is modeled by the Tight-Binding Approximation (TBA) which implies:

$$\mathbf{P} = \frac{\partial H_0}{\partial \mathbf{k}} - i[\mathbf{D}^{(\text{W})}(\mathbf{k}), H_0(\mathbf{k})]. \quad (\text{B4})$$

Using Eq. (B4), Eq. (B1) becomes sum rule,

$$i\delta_{\alpha\beta} I = i \frac{\partial^2 \hat{H}_0}{\partial k_\alpha \partial k_\beta} + \frac{\partial}{\partial k_\alpha} [\hat{D}^\beta, \hat{H}_0] + \left[\hat{D}^\alpha, \frac{\partial \hat{H}_0}{\partial k_\beta} \right] + i[\hat{D}^\beta, \hat{H}_0] \hat{D}^\alpha. \quad (\text{B5})$$

If we use condition $\mathbf{D}^{(\text{W})}(\mathbf{k}) = \mathbf{0}$, sum rule in Wannier representation becomes

$$\delta_{\alpha\beta} I = \frac{\partial^2 H_0}{\partial k_\alpha \partial k_\beta}, \quad (\text{B6})$$

which is only valid when $H_{mn} \approx \frac{1}{2} k^2 \delta_{mn}$, free-electron case. This shows that sum rule is always broken with above condition, therefore, the laser-electromagnetic gauge-symmetry too.

2. Conversion between electromagnetic gauge

We can convert operators in both gauge as [43]

$$\hat{O}^{(\text{VG})}(\mathbf{k}) = \hat{O}^{(\text{LG})}(\mathbf{k} + \mathbf{A}(t)). \quad (\text{B7})$$

However, the form of the operator $\hat{O}^{(\text{VG})}(\mathbf{k})$ is straightforward; the matrix form of relationship between the density matrices of the VG and LG is complicated [42, 45].

$$\hat{O}^{(\text{LG})}(\mathbf{k} + \mathbf{A}) = R(\mathbf{k}, \mathbf{A}) \hat{O}^{(\text{VG})}(\mathbf{k}) R^\dagger(\mathbf{k}, \mathbf{A}), \quad (\text{B8a})$$

$$R_{mn}(\mathbf{k}, \mathbf{A}) \equiv \langle u_{m\mathbf{k}+\mathbf{A}} | u_n \mathbf{k} \rangle. \quad (\text{B8b})$$

In TBA, Eq. (B8) can be calculated by

$$R^{k,A} = \hat{U}^{k+A^\dagger} \hat{U}^k \quad (\text{B9})$$

where \hat{U}^k is unitary eigenvector matrix of unperturbed Hamiltonian \hat{H}_0 .

Appendix C: Effects of dephasing in length and velocity gauges

This appendix numerically studies the effects of the dephasing T_2 on the high harmonic generation (HHG) process for our topological Chern insulator.

Since already the phenomenological dephasing time, T_2 , can be considered an external term related to the scattering and thermal processes in a medium, T_2 acts differently in both gauges [42, 45].

These are the primary sources of discrepancies in breaking the laser-electromagnetic gauge-symmetry. To avoid this T_2 effect, one can convert their density matrix for each time step - convert VG density matrix to LG density matrix, apply dephasing time and come back to VG density matrix [42]. However, this procedure slows down the calculation speed of the HHG spectra in VG, e.g. the computational numbers of operations and the time spent on this calculation. The VG SBEs becomes even slower than length gauge SBEs. Nevertheless, when this is compared with the Wannier basis, VG still has its advantage since Wannier LG also needs transformation to apply T_2 .

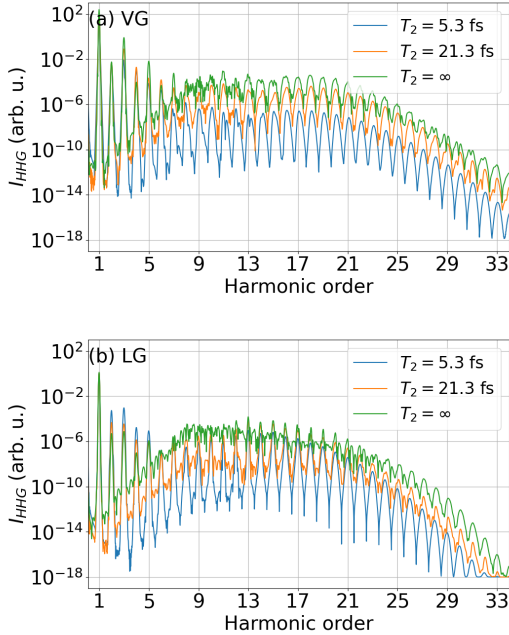


FIG. 11. Effect of T_2 for Chern insulator in LG and VG. HHG calculation results for (a) VG and (b) LG is shown. Laser is linearly polarized along $\Gamma - K$ direction, and laser parameters of Fig. 5 is used.

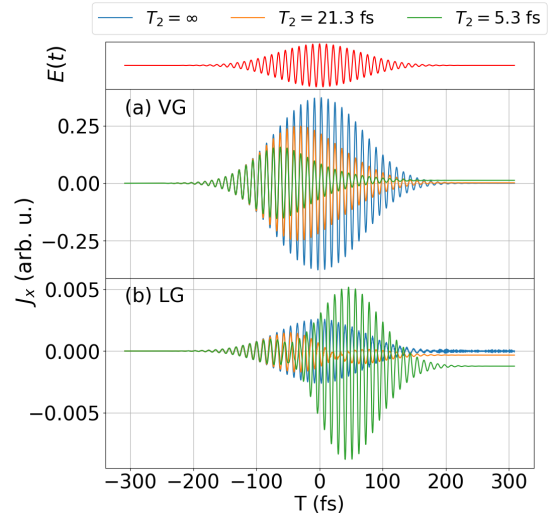


FIG. 12. Effect of T_2 for Chern insulator in length gauge and velocity gauge in current. Total current for (a) velocity gauge and (b) length gauge are shown. All the parameters are same as Fig. 11.

In Figs. 11(a) and 11(b) we depict the HHG spectra as a function of the phenomenological dephasing time T_2 for a topological Chern Insulator (CI). The perturbative region of the HHG spectra [1^{st} , 6^{th}] HOs shows different tendencies for both gauges. Significantly in the LG, the harmonic yield increases while the T_2 decreases for low HOs [23]. In contrast, we find that the VG provides opposite behavior than LG for low orders as a function of T_2 .

For the plateau and cut-off regions of the HHG spectra, the dephasing time T_2 induces a symmetry-gauge breaking in the spectrum of HHG too. Nevertheless, since T_2 in the VG and LG gauges reduce the noise in the emission signal, it is hard to quantify the difference between both gauges in Fig. 11. It is more obvious to observe the differences through current.

Figures 12 illustrate the effect of T_2 on the currents as a function of time. For VG, they act like a window function that removes the contribution from the later time domain. For LG, the effect is more complex and global. Noise at $T_2 = \infty$ is filtered, and envelope shape is also changed.

1. Computational complexities

We show brief illustration of computational cost for each method. In the case of LG SBEs, there are several choices like gradient or moving frame, but we will only mention the moving frame with tight binding model here. For both LG and VG SBEs, they have to calculate SBEs itself by matrix multiplication and addition and it costs about $f_{\text{SBEs}} = O(N_k N_b^3)$ by set matrix multiplication cost as $O(N_b^3)$. Here, N_k is total number of k-space grid and N_b is number of bands. LG SBEs have to calculate matrix elements at $\mathbf{K} + \mathbf{A}(t)$ for each time

step. Then it needs $f_{\text{GenMatrix}} = O(N_k N_b^2)$ order to generate appropriate matrices when assume that run time for calculate each components is $O(1)$. Then computation complexity for LG and VG SBEs without dephasing time is

$$f_{\text{LG}} = f_{\text{SBEs}} + f_{\text{GenMatrix}}, \quad (\text{C1})$$

$$f_{\text{VG}}^{\text{nodeph}} = f_{\text{SBEs}}. \quad (\text{C2})$$

If we include dephasing time, LG SBEs have almost no additional cost, but Wannier LG SBEs and VG have conversion cost about $f_{\text{dephasing}} = O(N_k N_b^3)$ which include generating eigenvector matrix and multiply this. Real cost for dephasing time in VG and Wannier LG is little bit different, but the difference is small enough. Then computational cost for Wannier or VG is

$$f_{\text{LG}}^{(W)} = f_{\text{SBEs}} + f_{\text{GenMatrix}} + f_{\text{dephasing}} \quad (\text{C3})$$

$$f_{\text{VG}} = f_{\text{SBEs}} + f_{\text{dephasing}}. \quad (\text{C4})$$

-
- [1] M. König, S. Wiedmann, C. Brüne, A. Roth, H. Bühmann, L. W. Molenkamp, X.-L. Qi, and S.-C. Zhang, *Science* **318**, 766 (2007), <https://arxiv.org/abs/0710.0582>.
- [2] B. A. Bernevig, T. L. Hughes, and S.-C. Zhang, *Science* **314**, 1757 (2006), <https://arxiv.org/abs/cond-mat/0611399>.
- [3] H. Zhang, C.-X. Liu, X.-L. Qi, X. Dai, Z. Fang, and S.-C. Zhang, *Nature Physics* **5**, 438 (2009), [arXiv:1405.2036](https://arxiv.org/abs/1405.2036).
- [4] Y. L. Chen, J. G. Analytis, J.-H. Chu, Z. K. Liu, S.-K. Mo, X. L. Qi, H. J. Zhang, D. H. Lu, X. Dai, Z. Fang, S. C. Zhang, I. R. Fisher, Z. Hussain, and Z.-X. Shen, *Science* **325**, 178 (2009), [arXiv:0904.1829v1](https://arxiv.org/abs/0904.1829v1).
- [5] S. A. Oliaei Motlagh, J. S. Wu, V. Apalkov, and M. I. Stockman, *Physical Review B* **98**, 125410 (2018).
- [6] M. Z. Hasan and C. L. Kane, *Rev. Mod. Phys.* **82**, 3045 (2010), <https://arxiv.org/abs/1002.3895>.
- [7] X.-L. Qi and S.-C. Zhang, *Rev. Mod. Phys.* **83**, 1057 (2011), <https://arxiv.org/abs/1008.2026>.
- [8] D. Xiao, M. C. Chang, and Q. Niu, *Reviews of Modern Physics* **82**, 1959 (2010), [arXiv:0907.2021](https://arxiv.org/abs/0907.2021).
- [9] D. Haddad, F. Seifert, L. S. Chao, S. Li, D. B. Newell, J. R. Pratt, C. Williams, and S. Schlamminger, *Rev. Sci. Instrum.* **87**, 061301 (2016).
- [10] H.-H. Kung, A. P. Goyal, D. L. Maslov, X. Wang, A. Lee, A. F. Kemper, S.-W. Cheong, and G. Blumberg, *Proceedings of the National Academy of Sciences* **116**, 4006 (2019), <https://www.pnas.org/content/116/10/4006.full.pdf>.
- [11] C. L. Kane and E. J. Mele, *Phys. Rev. Lett.* **95**, 226801 (2005), <https://arxiv.org/abs/cond-mat/0411737>.
- [12] J. M. Kosterlitz, *Rev. Mod. Phys.* **89**, 040501 (2017).
- [13] D. Shin, S. A. Sato, H. Hübener, U. D. Giovannini, J. Kim, N. Park, and A. Rubio, *Proceedings of the National Academy of Sciences* **116**, 201816904 (2019).
- [14] F. D. M. Haldane, *Phys. Rev. Lett.* **61**, 2015 (1988).
- [15] A. Chacón, D. Kim, W. Zhu, S. P. Kelly, A. Dauphin, E. Pisanty, A. S. Maxwell, A. Picón, M. F. Ciappina, D. E. Kim, C. Ticknor, A. Saxena, and M. Lewenstein, *Physical Review B* **102**, 134115 (2020).
- [16] M. Kohmoto, *Ann. Phys.* **160**, 343 (1985).
- [17] D. Bauer and K. K. Hansen, *Physical Review Letters* **120**, 177401 (2018), [arXiv:1711.05783](https://arxiv.org/abs/1711.05783).
- [18] H. Drüeke and D. Bauer, *Phys. Rev. A* **99**, 053402 (2019), <https://arxiv.org/abs/1901.01437>.
- [19] D. Baykuseva, A. Chacón, D. Kim, D. E. Kim, D. A. Reis, and S. Ghimire, *Phys. Rev. A* **103**, 023101 (2021).
- [20] J. W. McIver, B. Schulte, F.-U. Stein, T. Matsuyama, G. Jotzu, G. Meier, and A. Cavalleri, *Nature Phys.* **41**, 38 (2020).
- [21] R. E. F. Silva, B. Amorim, O. Smirnova, M. Ivanov, Á. Jiménez-Galán, B. Amorim, O. Smirnova, and M. Ivanov, *Nature Photonics* (2019), [10.1038/s41566-019-0516-1](https://doi.org/10.1038/s41566-019-0516-1).
- [22] R. E. F. Silva, A. Jiménez-Galán, B. Amorim, O. Smirnova, and M. Ivanov, *Nat. Photon.* **13**, 849 (2019), <https://arxiv.org/abs/1806.11232>.
- [23] G. Vampa, C. R. McDonald, G. Orlando, D. D. Klug, P. B. Corkum, and T. Brabec, *Phys. Rev. Lett.* **113**, 073901 (2014), http://www.attoscience.ca/pdf/Vampa_PRL_2014.pdf.
- [24] R. E. F. Silva, F. Martín, and M. Ivanov, *Phys. Rev. B* **100**, 195201 (2019).
- [25] G. B. Ventura, D. J. Passos, J. M. B. Lopes dos Santos, J. M. Viana Parente Lopes, and N. M. R. Peres, *Phys. Rev. B* **96**, 035431 (2017).
- [26] S. Ghimire, A. D. DiChiara, E. Sistrunk, P. Agostini, L. F. DiMauro, and D. A. Reis, *Nat. Phys.* **7**, 138 (2011), <http://www.dimauro.osu.edu/node/299>.
- [27] K. S. Virk and J. E. Sipe, *Physical Review B* **76**, 035213 (2007).
- [28] S. Y. Kruchinin, M. Korbman, and V. S. Yakovlev, *Physical Review B* **87**, 115201 (2013).
- [29] V. S. Yakovlev and M. S. Wismer, *Computer Physics Communications* **217**, 82 (2017).
- [30] C. Granados and L. Plaja, *Phys. Rev. A* **85**, 053403 (2012).
- [31] J. A. Pérez-Hernández, L. Roso, and L. Plaja, *Laser Phys.* **19**, 1581 (2009), <https://doi.org/10.1134/S1054660X0915033X>.
- [32] A. Chacón, M. F. Ciappina, and M. Lewenstein, *Phys. Rev. A* **92**, 063834 (2015).
- [33] E. Cormier and P. Lambropoulos, *Journal of Physics B: Atomic, Molecular and Optical Physics* **29**, 1667 (1996).
- [34] K. Amini, J. Biegert, F. Calegari, A. Chacón, M. F. Ciappina, A. Dauphin, D. K. Efimov, C. F. de Morisson Faria, K. Giergiel, P. Gniewek, A. S. Landsman, M. Lesiuk, M. Mandrysz, A. S. Maxwell, R. Moszyński, L. Ortmann, J. A. Pérez-Hernández, A. Picón, E. Pisanty, J. Prauzner-Bechcicki, K. Sacha, N. Suárez, A. Zaïr, J. Zakrzewski, and M. Lewenstein, *Reports on Progress in Physics* **82**, 116001 (2019).
- [35] L. Yue and M. B. Gaarde, *Phys. Rev. A* **101**, 053411 (2020).
- [36] E. Blount, in *Solid State Physics*, Vol. 13, edited by F. Seitz and D. Turnbull (Academic Press, 1962) pp. 305–373.
- [37] G. Vampa and T. Brabec, *J. Phys. B: At. Mol. Opt. Phys.* **50**, 083001 (2017).

- [38] R. E. Silva, F. Martín, and M. Ivanov, *Physical Review B* **100**, 1 (2019), [arXiv:1904.00283](https://arxiv.org/abs/1904.00283).
- [39] X. Wang, J. R. Yates, I. Souza, and D. Vanderbilt, *Phys. Rev. B* **74**, 195118 (2006).
- [40] N. Tancogne-Dejean, M. J. T. Oliveira, X. Andrade, H. Appel, C. H. Borca, G. Le Breton, F. Buchholz, A. Castro, S. Corni, A. A. Correa, U. De Giovannini, A. Delgado, F. G. Eich, J. Flick, G. Gil, A. Gomez, N. Helbig, H. Hübener, R. Jestädt, J. Jornet-Somoza, A. H. Larsen, I. V. Lebedeva, M. Lüders, M. A. L. Marques, S. T. Ohlmann, S. Pipolo, M. Rampp, C. A. Rozzi, D. A. Strubbe, S. A. Sato, C. Schäfer, I. Theophilou, A. Welden, and A. Rubio, *The Journal of Chemical Physics* **152**, 124119 (2020).
- [41] Y. C. Han and L. B. Madsen, *Physical Review A* **81** (2010), [10.1103/PhysRevA.81.063430](https://doi.org/10.1103/PhysRevA.81.063430).
- [42] L. Yue and M. B. Gaarde, *Phys. Rev. A* **101**, 53411 (2020).
- [43] G. B. Ventura, D. J. Passos, J. M. Lopes Dos Santos, J. M. Viana Parente Lopes, and N. M. Peres, *Physical Review B* **96** (2017), [10.1103/PhysRevB.96.035431](https://doi.org/10.1103/PhysRevB.96.035431).
- [44] N. Marzari and D. Vanderbilt, *Phys. Rev. B* **56**, 12847 (1997).
- [45] G. Ernotte, T. J. Hammond, and M. Taucer, *Physical Review B* **98**, 235202 (2018).